A Tunguska sized airburst destroyed Tall el-Hammam a Middle Bronze Age city in the Jordan Valley near the Dead Sea

Ted E. Bunch, Malcolm A. LeCompte, A. Victor Adedeji, James H. Wittke, T. David Burleigh, Robert E. Hermes, Charles Mooney, Dale Batchelor, Wendy S. Wolbach, Joel Kathan, Gunther Kletetschka, Mark C.L. Patterson, Edward C. Swindel, Timothy Witwer, George A. Howard, Siddhartha Mitra, Christopher R. Moore, Kurt Langworthy, James P. Kennett, Allen West, Phillip J. Silvia.

SUPPORTING INFORMATION

SUPPORTING INFORMATION, IMAGES

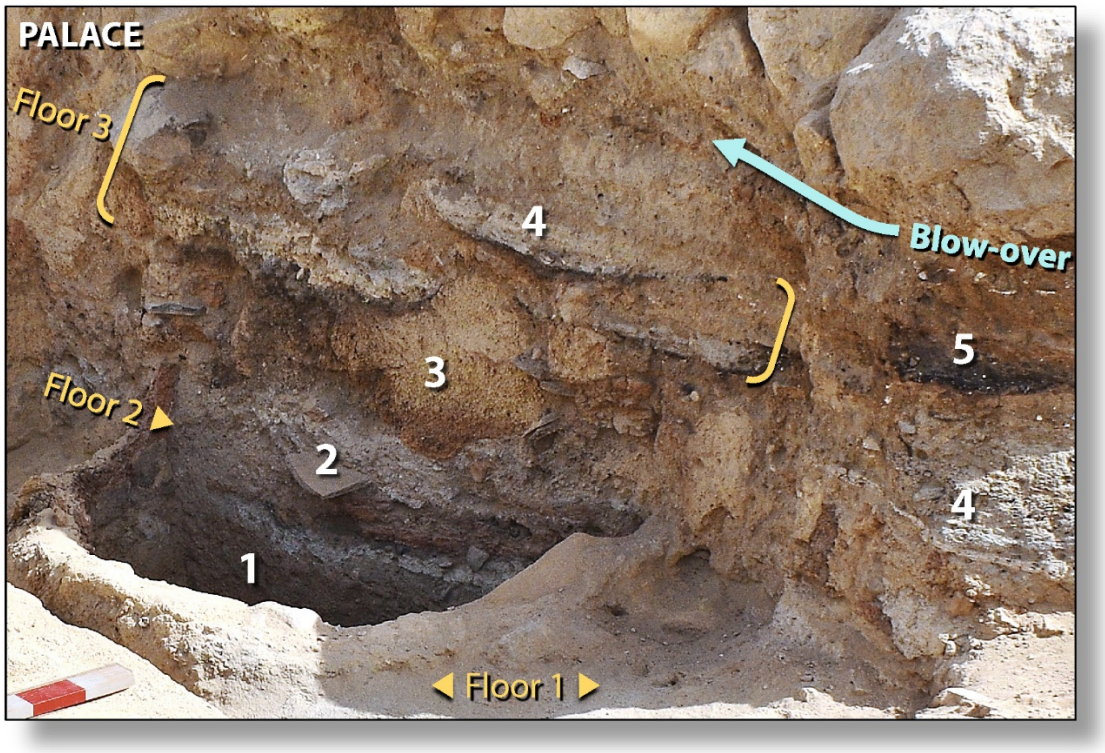

Figure S1. Collapsed multi-storied palace. Photo showing jumbled remains of three stories of the palace; the fourth story is completely missing. #1 represents a circular clay MBA oven called a tabun. #2 is a broken potsherd. #3 represents broken and burned mudbricks from the upper walls. #4 represents sections of burned roofing and upper-story flooring material. #5 represents charred wood from upper stories. The 'blow-over' layer capped and sealed the destroyed palace, which lay undisturbed for ~600 years. One-meter scale stick shown with 10-cm markings.

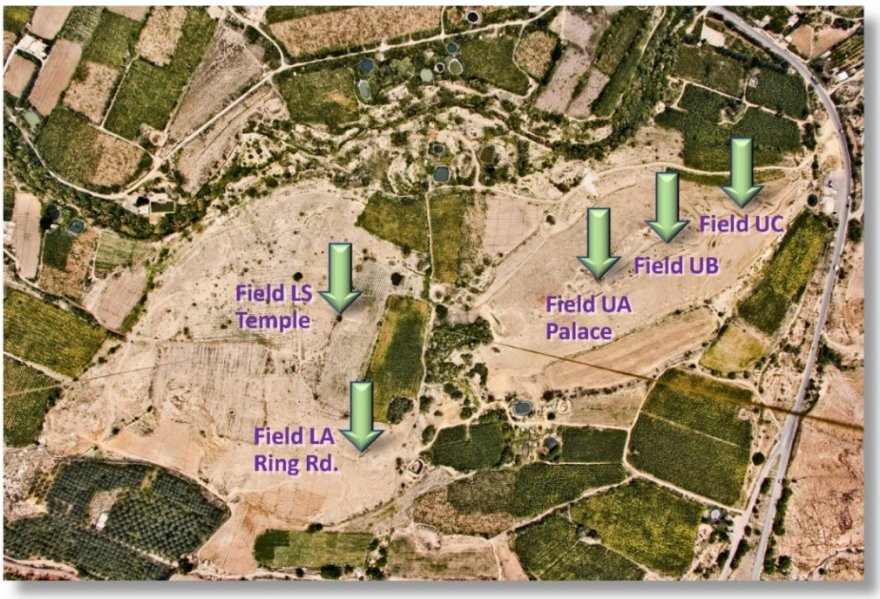

Figure S2. Tall el-Hammam showing main excavated areas. Relevant field areas in the main manuscript at arrows are Field LA = ring road near the main gate for the lower tall; Field LS = temple complex on the lower tall; and Fields UA, UB, UC = palace complex on the upper tall. The wadi site is not shown. Source of base image: "Tall el-Hammam." 31° 50.483, N 35° 40.029 E. Google Earth; CNES/Airbus. Imagery date: 11/26/2019; accessed: 4/4/2021. Permissions: https://about.google/brand-resource-center/products-and-services/geo-guidelines/ Modified by the authors using Adobe Photoshop CC2014 (adobe.com/ products/ photoshop.html).

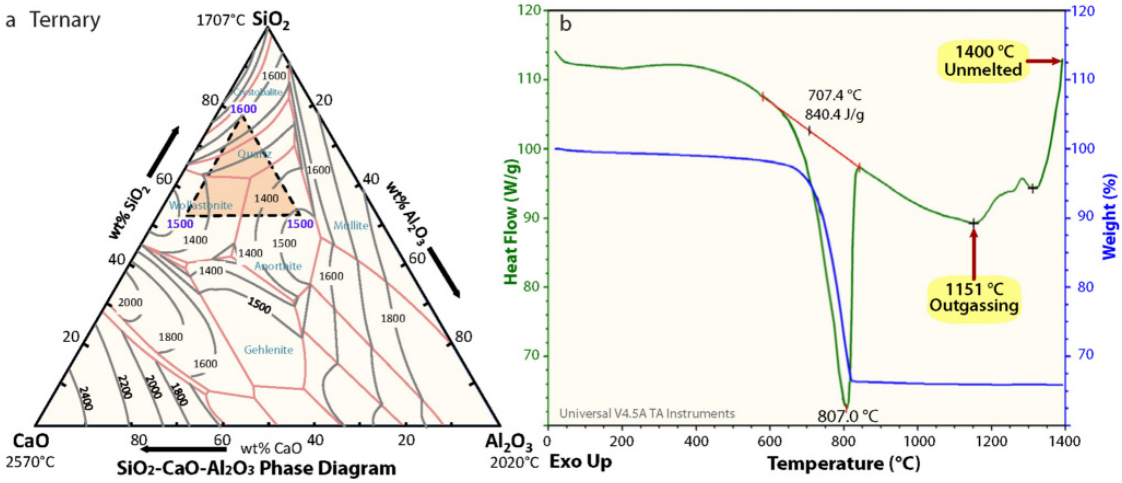

Figure S3. Experimental melting of pottery and mudbrick. (a) CaO-Al_2O_3-SiO_2 (CAS) ternary phase diagram showing the theoretical melting point of pottery and mudbrick at ~1300° to 1500°C, depending upon composition (base diagram, Metallos[1]). These are theoretical minimums and not maximum temperatures. **(b)** Thermal behavior of TeH pottery using Simultaneous Differential Scanning Calorimetry-Thermogravimetric Analysis (DSC-TGA). Furnace temperature ranged from ambient to 1400°C at 10°C/minute under argon purge. Powdered pottery showed a change of phase at 1151°C but no evidence of melting at the maximum temperature of ~1400°C.

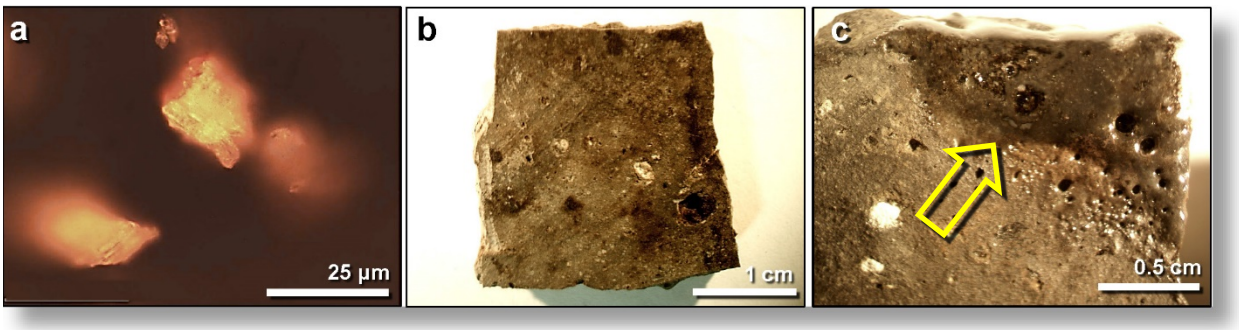

Figure S4. Pottery heating experiment images. (a) Photomicrograph of thermally unaltered pulverized pottery after exposure to 1400°C. Heating experiments used Differential Scanning Calorimetry with Thermogravimetric Analysis (DSC-TGA). **(b)** Unmelted potsherd from palace prior to the oxygen/propylene torch experiment. **(c)** Melted upper corner (arrow) of the same potsherd as in panel 'b' after exposure to temperatures of ~1500° ± 25°C for ~2 minutes.

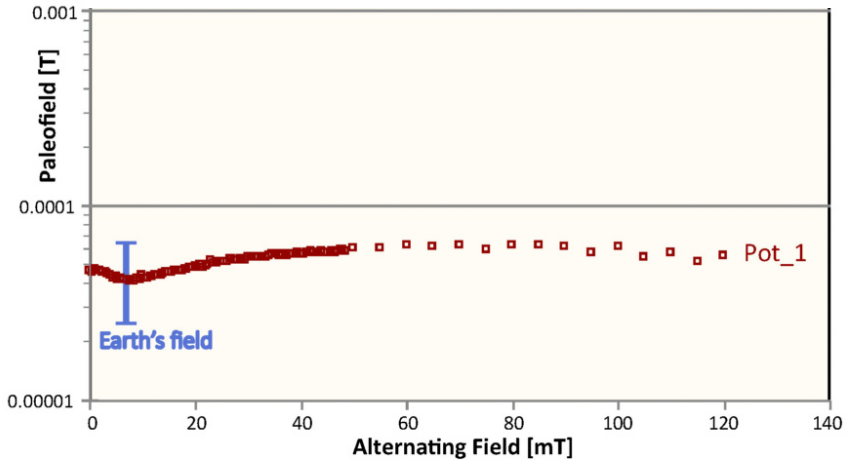

Figure S5. Remanent magnetism measurements of melted material. Sample Pot_1 is a 20.6-g sample of melted pottery from the palace. It shows paleo field measurements of <0.0001T, which is typical of cooling in Earth's geomagnetic field (blue bar shows Earth's field range of ~0.000025 to 0.000065T). These values indicate that the pottery was not melted by lightning.

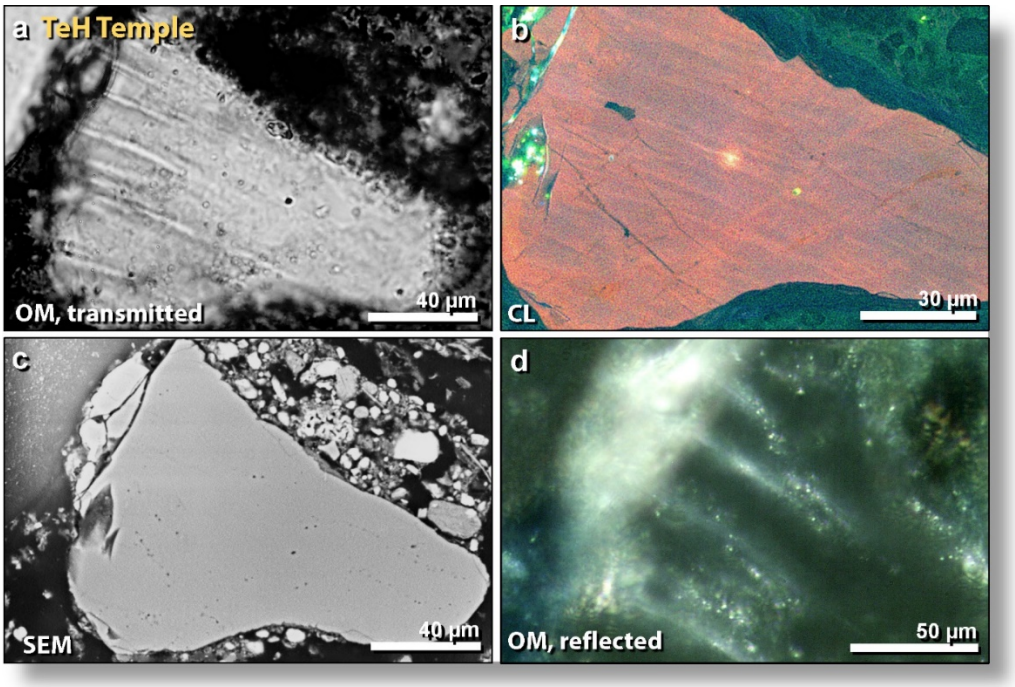

Figure S6. Images of a single tectonically-shocked quartz grain. (a) Transmitted light photomicrograph (optical microscopy, OM) of 170-µm-wide temple quartz grain, generally accepted as tectonically shocked[2]. Lamellae appear thicker and more ribbon-like than impact-shocked lamellae. (b) SEM-CL image displaying red luminescence of lamellae, which is similar to some impact-shocked material. However, tectonic lamellae are never black, indicative of non-luminescence, as often found in impact-shocked grains. (c) SEM image of same grain. Note that lamellae are not visible in SEM images, although some irregular micro-fractures are faintly visible. (d) Reflected light photomicrograph of same grain. Note that tectonic lamellae typically are thicker and less defined, but can be decorated with bubbles. Tectonic lamellae match only three of 17 features of shocked quartz grains.

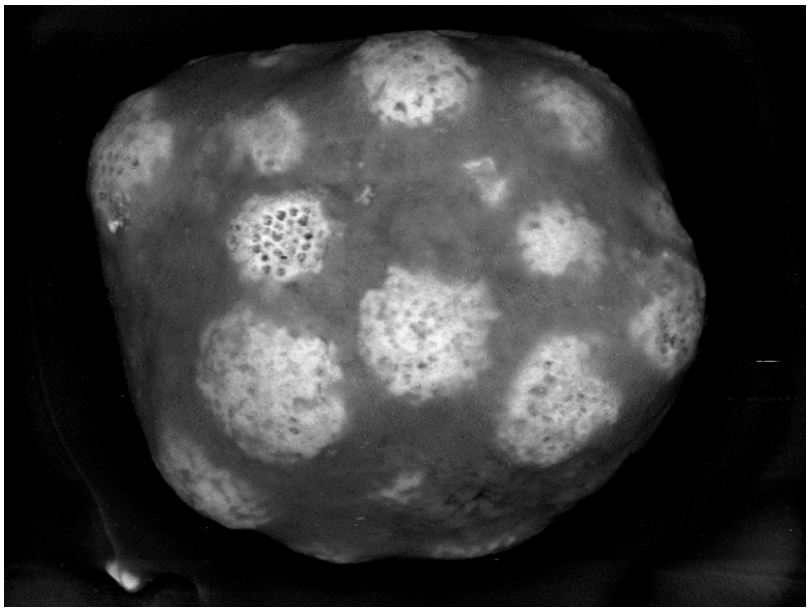

Figure S7. Framboid spherule (62-µm) from TeH. Spherulitic framboids are commonly observed in all TeH layers, including the destruction layer. These formed authigenically with time, and are thus unlikely to be related to the impact event.

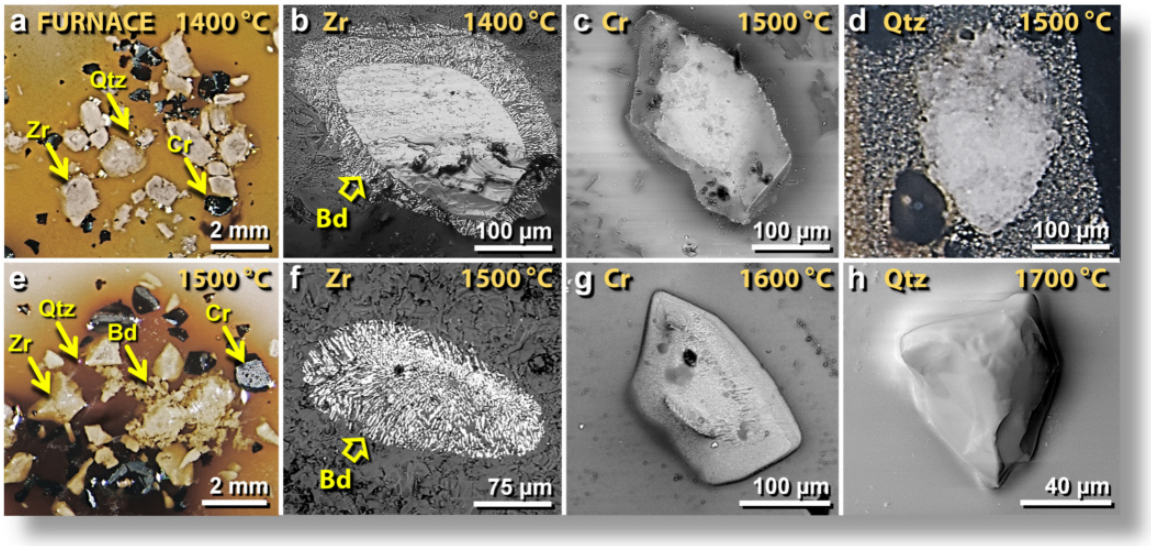

Figure S8. Grain images related to furnace heating experiments. (a) Photomicrograph shows that at ~1400°C, grains of zircon (Zr, at arrow), quartz (Qtz), and chromite (Cr) added to bulk sediment retained most of their original shapes. **(b)** SEM image of sectioned grain shows unaltered Zr at the center and incipient conversion to granular baddeleyite (Bd) around the outside at 1400°C. **(c)** SEM image of Cr minimally altered by temperatures of 1500°C. **(d)** Photomicrograph of sectioned Qtz unaltered at 1500°C. **(e)** At ~1500°C, the photomicrograph shows that Zr, Cr, and Qtz grains still mostly retain their original shapes, although some Zr has dissociated into granular baddeleyite (Bd). **(f)** SEM image of Zr grain completely converted to granular baddeleyite (Bd), as seen for Zr from the palace. **(g)** SEM image of Cr minimally altered by temperatures of 1600°C. **(h)** SEM image of euhedral Qtz grain showing no apparent thermal alteration at 1700°C, near its melting point of 1713°C. Images from Moore et al.[3] usable under Creative Commons, CC by 4.0.

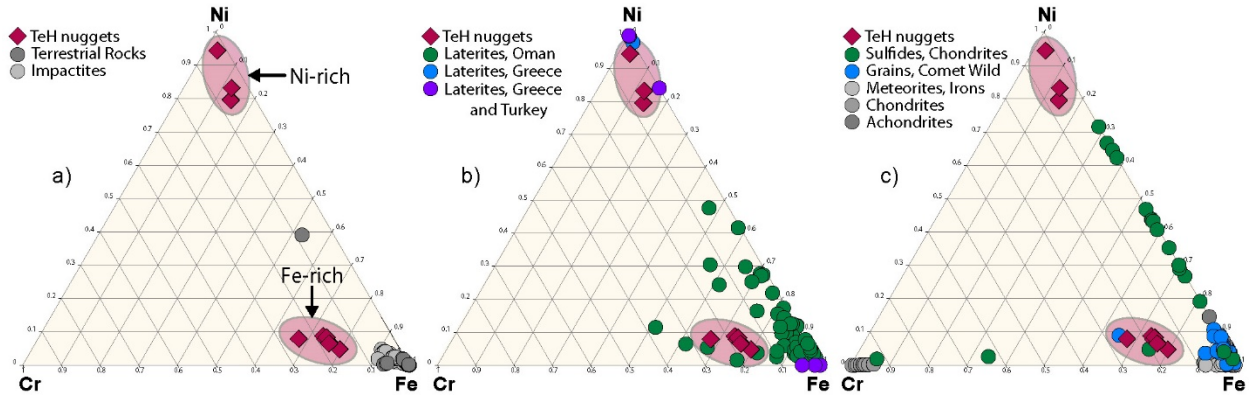

Figure S9. Ternary diagrams for meltglass grains enriched in Cr, Fe, and Ni. TeH samples are represented by red diamonds within light red ovals. There are two groups: one in which Ni>Fe>Cr in wt% and one in which Fe>Ni>Cr. ***(a)*** Both groups are chemically unlike typical terrestrial rocks and impactites produced by cosmic impacts. ***(b)*** The Ni-dominant group overlaps with Ni-laterites from Greece and Turkey; the Fe-dominant group overlaps Ni-laterites from Greece and Oman. ***(c)*** The Ni-dominant group is unlike meteoritic and cometary material; the Fe-dominant group overlaps with cometary grains and with Ni-sulfide inclusions in chondrites, but not with other meteoritic material.

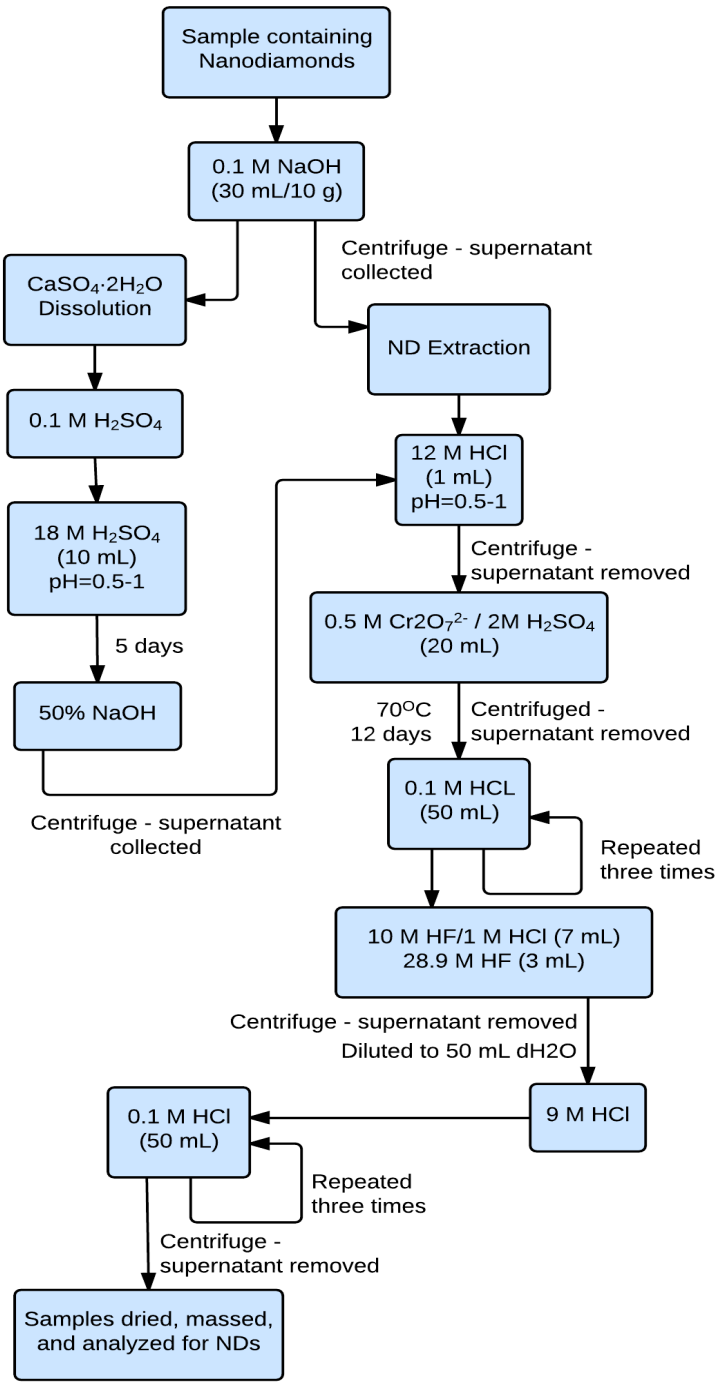

Figure S10. Flowchart showing the methods used for nanodiamond/diamonoid extraction.

SUPPORTING INFORMATION, TABLES

Table S1. Bayesian analysis of radiocarbon dates for destruction layer at TeH. 20 radiocarbon dates on material from the destruction layer. All dates are from the palace (Field UA). The Bayesian-calculated age is 1661 BCE ± 21 cal BP (3611 cal BP) for a likely range of 1686 to 1632 BCE at 68% CI. Calculated using the Combine feature of the OxCal program, version 4.4.3, IntCal20 calibration curve.

Tall el-Hammam			Unmodelled (BCE/CE)						Modelled (BCE/CE)						Indices	
	^{14}C	±	68% CI		95% CI				68% CI		95% CI					
20 ^{14}C dates			from	to	from	to	mu	sigma	from	to	from	to	mu	sigma	Acomb	A
Combine			-1686	-1632	-1689	-1628	-1661	21							143.6	
R_Date Beta-494574	3420	30	-1751	-1636	-1873	-1622	-1719	61	-1686	-1632	-1689	-1628	-1661	21		80.1
R_Date Beta-494577	3420	30	-1751	-1636	-1873	-1622	-1719	61	-1686	-1632	-1689	-1628	-1661	21		80.1
R_Date Beta-477409	3410	30	-1744	-1636	-1870	-1619	-1704	56	-1686	-1632	-1689	-1628	-1661	21		100.5
R_Date Beta-494575	3400	30	-1739	-1631	-1866	-1615	-1690	52	-1686	-1632	-1689	-1628	-1661	21		114.1
R_Date Beta-494576	3400	30	-1739	-1631	-1866	-1615	-1690	52	-1686	-1632	-1689	-1628	-1661	21		114.1
R_Date Beta-589019	3400	30	-1739	-1631	-1866	-1615	-1690	52	-1686	-1632	-1689	-1628	-1661	21		114.1
R_Date Beta-490628	3390	30	-1736	-1626	-1863	-1564	-1679	49	-1686	-1632	-1689	-1628	-1661	21		122
R_Date Beta-589000	3390	30	-1736	-1626	-1863	-1564	-1679	49	-1686	-1632	-1689	-1628	-1661	21		122
R_Date Beta-589016	3390	30	-1736	-1626	-1863	-1564	-1679	49	-1686	-1632	-1689	-1628	-1661	21		122
R_Date Beta-589020	3390	30	-1736	-1626	-1863	-1564	-1679	49	-1686	-1632	-1689	-1628	-1661	21		122
R_Date Beta-494573	3380	30	-1733	-1623	-1747	-1544	-1667	49	-1686	-1632	-1689	-1628	-1661	21		126.7
R_Date Beta-589001	3380	30	-1733	-1623	-1747	-1544	-1667	49	-1686	-1632	-1689	-1628	-1661	21		126.7
R_Date Beta-484763	3370	30	-1733	-1617	-1743	-1542	-1655	50	-1686	-1632	-1689	-1628	-1661	21		128.6
R_Date Beta-490631	3370	30	-1733	-1617	-1743	-1542	-1655	50	-1686	-1632	-1689	-1628	-1661	21		128.6
R_Date Beta-589006	3370	30	-1733	-1617	-1743	-1542	-1655	50	-1686	-1632	-1689	-1628	-1661	21		128.6
R_Date Beta-589007	3370	30	-1733	-1617	-1743	-1542	-1655	50	-1686	-1632	-1689	-1628	-1661	21		128.6
R_Date Beta-589008	3370	30	-1733	-1617	-1743	-1542	-1655	50	-1686	-1632	-1689	-1628	-1661	21		128.6
R_Date Beta-494579	3350	30	-1686	-1545	-1736	-1536	-1625	53	-1686	-1632	-1689	-1628	-1661	21		103.1
R_Date Beta-589017	3350	30	-1686	-1545	-1736	-1536	-1625	53	-1686	-1632	-1689	-1628	-1661	21		103.1
R_Date Beta-494580	3330	30	-1624	-1540	-1687	-1517	-1595	47	-1686	-1632	-1689	-1628	-1661	21		39.7

Table S2. Radiocarbon dates for Tall el-Hammam. Lab I.D.; radiocarbon dates and errors; Bayesian status ('Accepted'; rejected as 'too old'; or rejected as 'too young'); and source.

Lab I.D.	14C	±	Material	Bayesian	Source
Beta-589002	3480	30	carbonized wood	Too old	This paper
Beta-490632	3460	30	carbonized wood	Too old	This paper
Beta-589018	3430	30	carbonized grass	Too old	This paper
Beta-494574	3420	30	carbonized wood	Accepted	This paper
Beta-494577	3420	30	carbonized wood	Accepted	This paper
Beta-477409	3410	30	carbonized wood	Accepted	This paper
Beta-494575	3400	30	carbonized wood	Accepted	This paper
Beta-494576	3400	30	carbonized wood	Accepted	This paper
Beta-589019	3400	30	carbonized material	Accepted	This paper
Beta-490628	3390	30	burned bone	Accepted	This paper
Beta-589000	3390	30	carbonized wood	Accepted	This paper
Beta-589016	3390	30	carbonized material	Accepted	This paper
Beta-589020	3390	30	carbonized wood	Accepted	This paper
Beta-494573	3380	30	carbonized wood	Accepted	This paper
Beta-589001	3380	30	carbonized grain	Accepted	This paper
Beta-484763	3370	30	organic sediment	Accepted	This paper
Beta-490631	3370	30	carbonized material	Accepted	This paper
Beta-589006	3370	30	carbonized wood	Accepted	This paper
Beta-589007	3370	30	carbonized wood	Accepted	This paper
Beta-589008	3370	30	carbonized wood	Accepted	This paper
Beta-494579	3350	30	carbonized grain	Accepted	This paper
Beta-589017	3350	30	carbonized material	Accepted	This paper
Beta-494580	3330	30	carbonized grain	Accepted	This paper
Beta-494581	3280	30	carbonized wood	Too young	This paper
Beta-588998	3080	30	carbonized wood	Too young	This paper
Beta-589010	3010	30	material inside jar	Too young	This paper

Table S3. Concentrations of impact-related proxies in samples from the 4 TeH sequences. Depths, sample thicknesses, and abundances of shocked quartz (Sh. Qtz; number per 2000 grains), spherules (Spher.; # per kg), meltglass (Meltglass; g per kg), platinum (Pt; ppb), platinum/palladium ratio (Pt/Pd), loss-on-ignition (LOI), diamonoids (Diam.), gold, and salinity (Salt). Notes: (i) meltglass was collected from two closely-spaced locations at the palace 7GG and 7HH site; (ii) the wadi revealed no detectable meltglass; (iii) for the temple, two sampling sites (LS42J and LS42K) are close together (<4 m apart) and are reported together. (iv) all samples were contiguous except for one sample from the wadi.

Palace, Field UA, Square 7GG — **28-cm profile**

Samples	Depth, bott	Depth, top	Thick	Spher.	$CaCO_3$ Spher.	Melt-glass	Pt	Pt/Pd	Gold	Ir	Sh. Qtz	LOI	Salinity
name	cm (nom)	cm (actual)	cm	#/kg	#/kg	g/kg	ppb	ratio	ppb	ppb	#/2k gr	%	%
7GG-5	16	342	5	0	0	0	0.1	1	2.1	<0.1	0	21.6	<1
7GG-6	3	347	13	0	64k	0	0.1	1	3.5	<0.1	0	25.0	<1
7GG-7	0	360	3	310	240k	5-150	1.0	10	4.1	<0.1	3	42.7	4.0
7GG-8	-3	363	3	0	49k	0	0.1	1	2.5	<0.1	0	24.6	<1
7GG-9	-7	366	4	0	55k	0	0.1	1	3.0	<0.1	0	22.6	<1

Temple, Field LS, Square 42K — **43-cm profile**

Samples	Depth, bott	Depth, top	Thick	Spher.	$CaCO_3$ Spher.	Melt-glass	Pt	Pt/Pd	Gold	Ir	Sh. Qtz	Salinity
name	cm (nom)	cm (actual)	cm	#/kg	#/kg	g/kg	ppb	ratio	ppb	ppb	#/2k gr	%
LS42J-2	14	40	6	0	0	0	0.8	2.7	3.1	<0.1	0	<1
LS42J-3	6	46	8	0	150	0	0.2	0.7	2.5	<0.1	0	<1
LS42J-4	0	54	6	2345	420	0.1	4.2	5.3	3.0	<0.1	4	3.9
LS42J-5	-7	60	7	782	0	0	0.3	0.8	2.4	<0.1	0	<1
LS42J-6	-23	67	16	0	0	0	0.7	1.8	2.3	<0.1	0	<1

Ring Road, Field LA, Square 28M — **30-cm profile**

Samples	Depth, bott	Depth, top	Thick	Spher.	$CaCO_3$ Spher.	Melt-glass	Pt	Pt/Pd	Gold	Ir	Salinity
name	cm (nom)	cm (actual)	cm	#/kg	#/kg	g/kg	ppb	ratio	ppb	ppb	%
RR06	20	22	5	0	--	0	0.7	2.6	0	<0.1	<1
RR01	15	27	5	0	--	0	0.7	2.6	0	<0.1	2.7
RR02	10	32	5	0	0	0	0.7	2.6	0	<0.1	2.6
RR03	5	37	5	0	0	0	0.8	4.0	1.1	<0.1	2.8
RR04	0	42	5	2150	60	0.60	2.7	13.5	3.1	<0.1	2.9
RR05	-5	47	5	0	15	0.01	0.6	3.0	0	<0.1	2.9

Wadi — **130-cm profile**

Samples	Depth, bott	Depth, top	Thick	Spher.	$CaCO_3$ Spher.	Melt-glass	Pt	Pt/Pd	Gold	Ir	Salinity
name	cm (nom)	cm (actual)	cm	#/kg	#/kg	g/kg	ppb	ratio	ppb	ppb	%
WAR02	50	100	20	0	0	0	0.7	3.3	1.0	<0.1	<1
WAR03	30	130	10	0	70	0	0.6	1.7	0.9	0.5	<1
WAR04	0	160	10	2780	910	0	1.2	3.8	1.5	0.7	<1
WAR05	-20	180	10	0	0	0	0.7	0.5	1.0	1.0	<1
WAR06	-100	254	16	0	0	0	0.6	0.4	1.0	--	<1

Table S4. Chemical composition of melted spherules, pottery, and mudbrick. Average, high, and low weight percentages of major and minor oxides. Acquired by SEM-EDS.

	Spherules			Melted Pottery			Melted Mudbrick		
	Avg	High	Low	Avg	High	Low	Avg	High	Low
C	--	--	--	--	--	--	14.1	25.9	0.0
Na_2O	1.1	5.6	0.0	3.3	11.0	1.1	0.7	1.9	0.0
MgO	3.5	6.9	0.0	4.4	5.7	3.7	3.1	5.2	0.0
Al_2O_3	7.8	15.6	0.0	15.0	17.1	11.0	2.5	6.3	0.0
SiO_2	20.9	45.2	1.0	48.6	55.2	42.7	48.1	73.3	27.4
P_2O_5	0.3	2.6	0.0	0.4	0.6	0.0	5.9	16.3	0.0
SO_3	0.5	2.6	0.0	0.6	1.3	0.0	0.5	2.0	0.0
K_2O	2.0	7.7	0.0	2.8	3.2	2.3	3.0	4.6	0.0
CaO	2.6	7.1	0.0	17.5	25.5	12.8	17.2	32.3	2.8
TiO_2	7.1	53.1	0.0	0.1	1.5	0.8	0.2	0.8	0.0
MnO	0.0	0.7	0.0	0.1	0.4	0.0	0.2	2.4	0.0
FeO	40.2	84.1	0.0	6.4	7.5	5.6	4.6	13.4	0.0
Fe, nat	7.8	80.3	0.0	--	--	--	--	--	--
La_2O_3	2.1	28.7	0.0	--	--	--	--	--	--
CeO_2	4.1	70.8	0.0	--	--	--	--	--	--

Table S5. Oxide weight percentages of melted pottery. Microprobe spot measurements of a polished thin-sectioned piece of melted pottery from the palace, Field UA, Square 7GG. Acquired using microprobe analyses.

Formula	K2O	MgO	CaO	FeO	Al2O3	SiO2	Misc.	Total
Tehep-01	2.2	4.0	26.1	5.1	14.2	43.8	4.6	100.0
Tehep-02	1.8	4.9	24.8	5.4	12.8	45.5	4.8	100.0
Tehep-03	1.6	4.5	25.9	5.4	11.7	45.6	5.3	100.0
Tehep-04	2.4	4.1	23.6	5.8	13.1	46.9	4.1	100.0
Tehep-05	2.3	3.8	19.5	6.1	14.1	45.7	8.5	100.0
Tehep-06	2.5	3.7	20.4	5.8	12.8	44.6	10.2	100.0
Tehep-07	1.9	3.0	21.2	4.9	16.0	49.4	3.6	100.0
Tehep-08	2.8	3.2	16.3	6.5	14.7	43.8	12.7	100.0
Tehep-09	2.7	3.2	18.5	5.6	12.2	44.0	13.8	100.0
Tehep-10	1.5	4.1	20.8	5.9	14.8	44.1	8.8	100.0
Tehep-11	2.9	2. 5	16.9	4 .9	17.0	51.4	11.8	100.0
Tehep-12	1.4	2. 5	20.7	5.5	18.7	47.4	6.3	100.0
Tehep-13	0.9	5.0	21.4	6.4	17.6	45.4	3.3	100.0
Tehep-14	1.3	2. 5	21.2	4.9	19.5	47.0	6.1	100.0
Tehep-15	0.9	4.7	23.4	7.9	15.2	43.3	4.6	100.0
Tehep-16	2.3	4.4	19.0	6.0	17.1	48.5	2.7	100.0
Tehep-17	1.4	2.9	21.0	5.3	19.3	46.5	3.6	100.0
Tehep-18	1.7	4.5	26.1	5.0	13.1	44.7	4.9	100.0
Tehep-19	1.6	3.4	29.7	4.8	13.7	41.7	5.1	100.0

Table S6. Elemental weight percentages for PGE-rich material from TeH. SEM-EDS weight percentages and Pt/Ir ratios for Fe, Ir, and Pt in nuggets and splatter from TeH. Low concentrations have high uncertainties (±100 wt%), and wt% >10 wt% have uncertainties of approximately ±10 wt%, making these result preliminary and indicating the need for further research.

Sample name	Type	µm	C	O	Na	Mg	Al	Si	P	K	Ca	Mn	Fe	Ni	Zr	Mo	Ru	Rh	Pd	Ag	Os	Ir	Pt	
Pt_05_1um	Pt-rich nugget	1	6.2	16.3	0.3	1.6	0.0	3.6	0.0	0.6	6.1	0.0	0.6	--	0.0	0.0	0.0	--	0.0	--	--	12.3	52.5	100.0
Pt_02_4um	Pt-rich nugget	4	6.8	21.8	0.0	1.1	0.4	2.5	0.0	0.9	9.2	0.0	1.2	--	14.2	0.0	0.0	--	0.0	--	--	8.0	34.0	100.0
Pt_02_4um	Pt-rich nugget	4	7.1	35.2	0.0	1.8	0.0	3.2	9.7	1.3	18.7	0.0	1.3	--	1.5	0.0	0.0	--	0.0	--	--	1.7	18.6	100.0
Pt_01_5um	Pt-rich nugget	5	9.2	39.1	0.0	3.2	1.3	9.0	0.0	0.9	8.0	0.0	1.2	--	8.5	0.0	0.0	--	0.0	--	--	0.0	19.6	100.0
Pt_06_12um	Pt-rich nugget	12	--	45.8	1.2	0.0	1.2	13.0	0.0	0.0	16.2	0.0	0.0	--	0.0	0.0	0.0	--	0.0	--	--	0.0	22.6	100.0
Pt_02_4um	Pt-rich nugget	4	7.2	22.6	0.0	1.2	0.4	2.7	0.0	0.8	8.5	0.0	1.1	--	19.2	0.0	0.0	--	0.0	--	--	6.3	30.0	100.1
Pt_01_5um	Pt-rich nugget	5	8.6	30.1	0.3	1.7	1.1	5.5	0.0	0.8	6.7	0.0	0.9	--	0.0	0.0	0.0	--	0.0	--	--	6.4	38.0	100.0
Pt_05_1um	Pt-rich nugget	1	7.4	18.0	0.3	1.6	0.0	3.7	0.0	0.6	6.1	0.0	0.6	--	11.1	0.0	0.0	--	0.0	--	--	9.5	41.0	100.0
Pt_01_5um	Pt-rich nugget	5	8.1	22.2	0.0	1.2	0.7	3.8	0.0	0.0	5.3	0.0	0.8	--	8.1	0.0	0.0	--	0.0	--	--	7.6	42.2	100.0
Pt_01_5um	Pt-rich nugget	5	7.2	21.5	0.0	1.2	0.8	3.8	0.0	0.6	5.2	0.0	0.7	--	6.8	0.0	0.0	--	0.0	--	--	7.6	44.7	100.0
Pt_01_5um	Pt-rich nugget	5	8.4	19.7	0.0	1.3	0.6	3.8	0.0	0.5	4.9	0.0	0.8	--	7.5	0.0	0.0	--	0.0	--	--	7.2	45.4	100.0
Pt_03_1um	Pt-rich nugget	1	8.2	23.5	0.3	1.2	0.5	3.2	0.0	0.7	8.3	0.8	1.2	--	0.0	0.0	2.2	--	0.0	--	--	3.9	46.0	100.0
Pt_02_5um	Pt-rich nugget	5	5.2	20.6	0.3	1.2	0.4	2.5	0.0	0.7	8.4	0.0	1.1	--	0.0	0.0	1.7	--	0.0	--	--	9.9	48.1	100.0
Pt_01_5um	Pt-rich nugget	5	7.8	22.6	0.2	1.4	0.7	4.3	0.0	0.5	4.6	0.0	0.8	--	0.0	0.0	0.0	--	0.0	--	--	7.4	49.7	100.0
Pt_01_5um	Pt-rich nugget	5	7.7	27.1	0.0	1.5	1.0	5.2	0.0	0.7	5.1	0.0	1.0	--	0.0	0.0	0.0	--	0.0	--	--	0.0	50.7	100.0
Pt_01_5um	Pt-rich nugget	5	7.5	14.4	0.0	1.0	0.4	2.9	0.0	0.4	3.9	0.0	0.7	--	9.1	0.0	0.0	--	0.0	--	--	8.3	51.4	100.0
Pt_01_5um	Pt-rich nugget	5	7.6	18.9	0.0	1.2	0.6	3.6	0.0	0.0	4.4	0.0	0.7	--	2.9	0.0	0.0	--	0.0	--	--	8.0	52.2	100.0
Pt_04_2um	Pt-rich nugget	2	5.2	14.7	0.2	1.0	0.3	2.3	0.0	0.7	6.0	0.0	1.2	--	0.0	0.0	2.5	--	0.0	--	--	6.1	59.8	100.0
Pt_06_12um	Pt-rich nugget	12	--	13.9	0.0	0.0	0.0	4.7	0.0	0.0	7.4	0.0	2.2	--	0.0	0.0	3.2	--	0.2	--	--	6.3	62.2	100.0
Pt_07_12um	Pt-rich nugget	12	5.3	10.0	0.0	0.7	0.0	2.2	0.0	0.6	4.5	0.0	1.3	--	0.0	0.0	3.7	--	0.1	--	--	4.5	67.1	100.0
Pt_06_12um	Pt-rich nugget	12	6.1	9.0	0.0	0.6	0.0	1.8	0.0	0.7	4.6	0.0	1.2	--	0.0	0.0	3.4	--	0.0	--	--	5.0	67.7	100.0
			7.2	**22.2**	**0.1**	**1.2**	**0.5**	**4.1**	**0.5**	**0.6**	**7.2**	**0.0**	**1.0**		**4.2**	**0.0**	**0.8**		**0.0**			**6.0**	**44.9**	
Pt_08_2um	Fe-rich splatter	2	--	48.5	0.0	0.0	0.0	18.4	3.3	0.0	15.5	0.0	6.8	--	0.0	0.0	0.2	--	0.0	--	--	0.5	7.0	100.0
Area_150um	Fe-rich splatter	150	--	53.8	--	--	5.9	31.3	--	--	5.1	--	2.1	0.0	--	0.0	0.0	0.0	0.1	--	0.5	0.9	0.3	100.0
Area_02_775um	Fe-rich splatter	775	--	49.2	--	--	5.8	16.7	--	--	10.3	--	6.2	0.5	--	1.1	0.0	0.0	0.1	--	0.2	8.6	1.6	100.0
Area_03_33um	Fe-rich splatter	33	--	45.5	--	--	2.1	15.0	--	--	6.7	--	25.6	0.1	--	0.2	0.0	0.0	0.1	--	0.0	4.4	0.5	100.0
Area_04_20um	Fe-rich splatter	20	--	34.7	--	--	1.7	11.1	--	--	9.5	--	35.7	0.3	--	0.2	0.0	0.0	0.2	--	0.0	6.0	0.7	100.0
Area_05_200um	Fe-rich splatter	200	--	40.6	--	--	2.4	9.6	--	--	8.7	--	34.4	0.1	--	0.1	0.0	0.0	0.0	--	0.0	3.7	0.5	100.0
Area_80um	Fe-rich splatter	80	--	49.5	--	--	3.1	27.4	--	--	7.5	--	3.9	0.1	--	0.3	0.0	0.0	0.0	--	0.0	7.4	0.8	100.0
Bleb_01_56um	Fe-rich splatter	56	--	38.0	--	--	3.2	18.1	--	--	7.1	--	25.5	0.2	--	0.0	0.0	0.1	0.2	--	0.0	6.6	1.0	100.0
				45.0	**0.0**	**0.0**	**3.0**	**18.4**	**3.3**	**0.0**	**8.8**	**0.0**	**17.5**	**0.2**	**0.0**	**0.2**	**0.0**	**0.0**	**0.1**		**0.1**	**4.7**	**1.5**	

Table S7. Elemental weight percentages various PGE-rich materials. SEM-EDS weight percentages for Fe, Ir, and Pt. The Pt-dominant nuggets and Fe-dominant splatter from TeH are compared to nuggets from terrestrial placer deposits, extraterrestrial carbonaceous chondrites, cosmic spherules, iron meteorites, and cometary nuggets. The Pt-dominant TeH nuggets best match nuggets from placer deposits, and the Fe-dominant splatter best matches extraterrestrial nuggets from carbonaceous chondrites, cosmic spherules, iron meteorites, and comets.

				Fe	Mo	Ir	Pt	
Samples	**Source**	**Type of**	**#**	**Avg**	**Avg**	**Avg**	**Avg**	**Matches**
Pt-dom. nuggets	TeH	Palace	21	1.0	0.0	6.0	44.9	Pt-dom. placer
Fe-dom. splatter	TeH	Palace	8	17.5	0.3	4.7	1.5	ET nuggets
Pt-dom. nuggets	Placers	Terrest.	109	8.2	0.0	2.9	80.3	Pt-dom. TeH
Ir-dom. nuggets	Placers	Terrest.	104	0.4	0.0	47.8	5.3	Pt-dom. TeH
PGE nuggets	Chondrites	ET	95	21.6	11.5	11.1	8.7	Fe-dom. TeH
PGE nuggets	Cosmic spher.	ET	53	12.3	0.6	18.3	19.2	Fe-dom. TeH
PGE nuggets	Iron meteorites	ET	12	6.2	0.0	18.2	19.5	Fe-dom. TeH
PGE nuggets	Comets	ET	4	56.8	5.8	7.6	12.4	Fe-dom. TeH

Table S8. Bayesian analysis of radiocarbon dates for destruction layer at Jericho. Compilation of 15 radiocarbon dates on material from the destruction layer at Jericho[4-6]. The Bayesian-calculated age is 1653 BCE ± 18 BCE (3603 cal BP) for a likely range (68% Confidence Interval) of 1670 to 1626 BCE at 68% CI. Calculated using the Combine feature of the OxCal program, version 4.4.3, IntCal20 calibration curve.

Jericho			Unmodelled (BCE/CE)						Modelled (BCE/CE)						Indices	
	14C	±	68% CI		95% CI				68% CI		95% CI					
			from	to	from	to	mu	sigma	from	to	from	to	mu	sigma	Acomb	A
Combine			-1670	-1626	-1683	-1623	-1653	18							149.1	
R_Date GL-33	3510	110	-2014	-1689	-2137	-1542	-1843	149	-1670	-1626	-1683	-1623	-1653	18		67.7
R_Date GrN-18368	3393	17	-1735	-1633	-1741	-1623	-1680	36	-1670	-1626	-1683	-1623	-1653	18		95.6
R_Date GrN-19223	3388	16	-1731	-1631	-1740	-1622	-1675	34	-1670	-1626	-1683	-1623	-1653	18		103.8
R_Date GrN-18721	3385	20	-1729	-1628	-1741	-1619	-1673	36	-1670	-1626	-1683	-1623	-1653	18		111.9
R_Date GrN-18537	3384	15	-1688	-1630	-1739	-1622	-1672	33	-1670	-1626	-1683	-1623	-1653	18		109.3
R_Date GrN-18370	3380	25	-1730	-1625	-1745	-1566	-1669	42	-1670	-1626	-1683	-1623	-1653	18		121.9
R_Date GrN-19064	3375	25	-1730	-1622	-1744	-1547	-1663	43	-1670	-1626	-1683	-1623	-1653	18		126.7
R_Date GL-56	3370	115	-1868	-1514	-1954	-1419	-1679	141	-1670	-1626	-1683	-1623	-1653	18		136.7
R_Date GrN-18722	3368	17	-1685	-1621	-1739	-1612	-1659	36	-1670	-1626	-1683	-1623	-1653	18		124.4
R_Date GrN-18363	3365	25	-1688	-1616	-1740	-1543	-1651	46	-1670	-1626	-1683	-1623	-1653	18		134
R_Date GrN-18365	3360	25	-1731	-1613	-1738	-1542	-1643	48	-1670	-1626	-1683	-1623	-1653	18		134
R_Date GL-52	3360	150	-1878	-1498	-2118	-1296	-1676	186	-1670	-1626	-1683	-1623	-1653	18		138.7
R_Date GrN-18367	3350	20	-1682	-1546	-1732	-1542	-1624	47	-1670	-1626	-1683	-1623	-1653	18		106.8
R_Date GrN-19068	3350	16	-1678	-1548	-1731	-1543	-1625	44	-1670	-1626	-1683	-1623	-1653	18		92.5
R_Date GL-64	3330	90	-1736	-1506	-1878	-1428	-1626	110	-1670	-1626	-1683	-1623	-1653	18		120.9
R_Date Rome-1176	3330	60	-1682	-1520	-1764	-1454	-1612	77	-1670	-1626	-1683	-1623	-1653	18		101.5

Table S9. Radiocarbon dates for Jericho. Lab I.D.; 27 radiocarbon dates and errors; Bayesian status ('accepted'; rejected as 'too old'; or rejected as 'too young'); and source. 3 dates are from Marchetti et al.[6], 6 are from Weinstein[5], and 18 are from Bruins and van der Plicht[4].

Lab I.D.	14C	±	Material	Bayesian	Source
GrN-18538	3614	20	Charcoal	Too old	Bruins, 1995
GL-33	3510	110	Wood	Accepted	Weinstein, 1984
GrN-18368	3393	17	Charcoal	Accepted	Bruins, 1995
GrN-19223	3388	16	Charcoal	Accepted	Bruins, 1995
GrN-18721	3385	20	Charcoal	Accepted	Bruins, 1995
GrN-18537	3384	15	Charcoal	Accepted	Bruins, 1995
GrN-18370	3380	25	Charcoal	Accepted	Bruins, 1995
GrN-19064	3375	25	Grains	Accepted	Bruins, 1995
GL-56	3370	115	Human remains	Accepted	Weinstein, 1984
GrN-18722	3368	17	Charcoal	Accepted	Bruins, 1995
GrN-18363	3365	25	Charcoal	Accepted	Bruins, 1995
GrN-18365	3360	25	Charcoal	Accepted	Bruins, 1995
GL-52	3360	150	Human remains	Accepted	Weinstein, 1984
GrN-18367	3350	20	Charcoal	Accepted	Bruins, 1995
GrN-19068	3350	16	Charcoal	Accepted	Bruins, 1995
GL-64	3330	90	Human remains	Accepted	Weinstein, 1984
Rome-1176	3330	60	Charcoal	Accepted	Marchetti, 2000
GrN-18536	3342	17	Charcoal	Too young	Bruins, 1995
GrN-18543	3331	18	Grains	Too young	Bruins, 1995
GrN-18539	3312	14	Grains	Too young	Bruins, 1995
GrN-18544	3312	15	Grains	Too young	Bruins, 1995
GrN-18542	3288	20	Grains	Too young	Bruins, 1995
GL-5	3270	110	Wood	Too young	Weinstein, 1984
GrN-19063	3240	18	Grains	Too young	Bruins, 1995
GL-30	3220	50	Human remains	Too young	Weinstein, 1984
Rome-1175	3110	60	Charcoal	Too young	Marchetti, 2000
BM-1790	3080	40	Charcoal	Too young	Marchetti, 2000

Table S10. Computer model of a theoretical airburst by 60-m Tunguska-Class impactor. The Online Impact Calculator program was developed by impact experts, J. Melosh, R. Marcus, and G. Collins[7,8], and is here used to estimate the airburst parameters and effects of a 75-m-wide Tunguska-class impactor. The result represents just one of many possible scenarios and has very large uncertainties. Nevertheless, the calculations are considered reasonable estimates and demonstrate that a Tunguska-like airburst can theoretically account for all the evidence observed at TeH.

AIRBURST by 60-m-wide ASTEROID or COMET
Parameters of Tunguska-class airburst event (Collins et al. 2005a, 2005b)
Average recurrence: every **1400 years**
Projectile diameter: **60 meters**
Projectile Density: rock at **~3000 kg/m^3**
Impact Velocity: **17 km/s or ~61,000 km/h**
Impact Angle: **45°** above horizon
Target: Unconsolidated sediment, density: **2500 kg/m^3**
Distance from palace complex: **~5 km**
Atmospheric Entry:
Object begins to breakup at an altitude of **54000 meters (540 km)**
Object bursts into cloud of fragments at height of **4.7 km**
The residual velocity of the fragments is **~17,200 km/h (10,700 mph)**
The energy of the airburst is **~12 Megatons**
No crater is formed, although large fragments may strike the surface
Modeled Airburst near Tall el-Hammam:
Max wind velocity on ground: **~255 m/s** or **917 km/h** or **570 mph**
Category 5 tornado force winds are **>320 km/h** (**>200 mph)**
>320 km/h is sufficient to pulverize mudbrick buildings on upper and lower tall
Traveling 5 km at this velocity, the shockwave will arrive **~21 seconds** after detonation
Wind velocity: Jericho ~15 km fm ground zero = **~237 km/h (~147 mph) = EF-3 tornado**
Sound Intensity: **108 dB**, ruptures eardrums, bursts blood vessels
Peak overpressure of up to **1.69-3.38 bars (24-48 psi)**
≥**0.14 MPa (20 psi)** >99% human fatality rate (Zipf and Cashdollar, 2007)
≥**0.14 MPa (20 psi)** Heavily-built buildings severly damaged or demolished (Zipf and Cashdollar, 2007)
0.24 MPa (**35 psi)** Exceeds tensile strength of mudbricks (adobe) (Silveiri, 2012)
0.24 MPa (35 psi) Exceeds flexural strength of mudbricks (adobe) (Clifton and Davis, 1979)
Thermal pulse from airburst **melt silicate minerals** and set flammable materials on fire
Temperatures approximately **>150°C** are lethal for humans and crops
Ground temperatures near the fireball rise to **>2000°C**

Table S11. Computer model of a theoretical airburst by 75-m Tunguska-Class impactor. The Online Impact Calculator program was developed by impact experts, J. Melosh, R. Marcus, and G. Collins[7,8], and is here used to estimate the airburst parameters and effects of a 75-m-wide Tunguska-class impactor. The result represents just one of many possible scenarios and has very large uncertainties. Nevertheless, the calculations are considered reasonable estimates and demonstrate that a Tunguska-like airburst can theoretically account for all the evidence observed at TeH.

AIRBURST by 75-m-wide ASTEROID or COMET
Parameters of Tunguska-class airburst event (Collins et al. 2005a, 2005b)
Average recurrence: every **2700 years**
Projectile diameter: **75 meters**
Projectile Density: rock at **~3000 kg/m^3**
Impact Velocity: **17 km/s or ~61,000 km/h**
Impact Angle: **45°** above horizon
Target: Unconsolidated sediment, density: **2500 kg/m^3**
Distance from palace complex: **~5 km**
Atmospheric Entry:
Object begins to breakup at an altitude of **54000 meters (540 km)**
Object bursts into cloud of fragments at height of **1.27 km**
The residual velocity of the fragments is **~12,700 km/h (7900 mph)**
The energy of the airburst is **~23 Megatons**
No crater is formed, although large fragments may strike the surface
Modeled Airburst near Tall el-Hammam:
Max wind velocity on ground: **~330 m/s** or **1200 km/h** or **740 mph**
Category 5 tornado force winds are **>320 km/h** (**>200 mph)**
>320 km/h is sufficient to pulverize mudbrick buildings on upper and lower tall
Traveling 5 km at this velocity, the shockwave will arrive **~16 seconds** after detonation
Wind velocity: Jericho ~15 km fm ground zero = **~216 km/h (~140 mph) = EF-3 tornado**
Sound Intensity: **108 dB**, ruptures eardrums, bursts blood vessels
Peak overpressure of up to **35 psi (2.5 bars or 0.24 MPa)**
≥0.14 MPa (20 psi) >99% human fatality rate (Zipf and Cashdollar, 2007)
≥0.14 MPa (20 psi) Heavily-built buildings severly damaged or demolished (Zipf and Cashdollar, 2007)
0.24 MPa (35 psi) Exceeds tensile strength of mudbricks (adobe) (Silveiri, 2012)
0.24 MPa (35 psi) Exceeds flexural strength of mudbricks (adobe) (Clifton and Davis, 1979)
Thermal pulse from airburst melt silicate minerals and set flammable materials **on fire**
Temperatures approximately **>150°C** are lethal for humans and crops
Ground temperatures near the fireball rise to **>2000°C**

SUPPORTING TEXT

Text S1. Archaeological periods and age ranges. General periods use the following abbreviations: Pre-Pottery Neolithic Period = PPNP; Pottery Neolithic Period = PNP; Chalcolithic Period = CP; Early Bronze Age = EBA; Intermediate Bronze Age = IBA; Middle Bronze Age = MBA; Late Bronze Age = LBA; Iron Age = IA; Hellenistic Period = HP; Early Roman Period = ERP; Late Roman Period = LRP; Byzantine Period = BP. Islamic Periods use traditional designations. We are applying the following general chronology of Collins et al.[9]:

PN1: Pottery Neolithic/early 6000-5500 BCE
PN2: Pottery Neolithic/middle 5500-5000 BCE
PN3: Pottery Neolithic/late 5000-4500 BCE
CH1: Chalcolithic/early 4500-4100 BCE
CH2: Chalcolithic/middle 4100-3800 BCE
CH3: Chalcolithic/late 3800-3500 BCE
EB1a: Early Bronze 1/early 3500-3350 BCE
EB1b: Early Bronze 1/middle 3350-3250 BCE
EB1c: Early Bronze 1/late 3250-3100 BCE
EB2a: Early Bronze II/early 3100-3000 BCE
EB2b: Early Bronze II/middle 3000-2900 BCE
EB2c: Early Bronze II/late 2900-2800 BCE
EB3a: Early Bronze III/early 2800-2650 BCE
EB3b: Early Bronze III/middle 2650-2500 BCE
EB3c: Early Bronze III/late 2500-2350 BCE
IB1: Intermediate Bronze/earlier 2350-2200 BCE (old EB IV)
IB2: Intermediate Bronze/later 2200-2000 BCE (old MB I)
MB1: Middle Bronze I 2000-1800 BCE (old MB IIA)
MB2: Middle Bronze II 1800-1550 BCE (old MB IIB-C)
LB1: Late Bronze I 1550-1400 BCE
LB2a: Late Bronze IIA 1400-1300 BCE
LB2b: Late Bronze IIB 1300-1200 BCE
IA1a: Iron IA 1200-1100 BCE
IA1b: Iron 1B 1100-1000 BCE
IA2a: Iron IIA 1000-900 BCE
IA2b: Iron IIB 900-700 BCE
IA2c: Iron IIA 700-539 BCE
IA3: Iron III/Persian Period 539-332 BCE
Hellenistic Period 332-63 BCE
Early Roman Period 63 BCE-135 CE

Text S2. Experimental melting of palace plaster. To investigate the melting point of calcium carbonate palace plaster during its potential conversion to spherules, we conducted laboratory experiments using an oxygen/propylene torch and thermocouple. Before heating, scratch testing showed that the unmelted plaster would scratch glass but not quartz, indicating a Mohs hardness of between 5.5 (glass) and 7 (quartz). After exposure for ~2 minutes, one fragment of unmelted plaster still retained its shape, but had a Mohs hardness of <1 and crumbled easily. Optical microscopy showed minimal melting at ~1500° ± 25°C, with small areas of the plaster

transitioning from opaque to translucent material. The maximum temperature of ~1500° ± 25°C was capable of melting mild steel, which was tested at the same time. Although the temperature and heat flux were sufficient for minimally melting small parts of the plaster, the experiment was unable to convert the plaster into spherules. This result suggests that the maximum exposure temperature for converting plaster to spherules is >1500°C and a higher flux rate is required.

Text S3. Comparison of severe damage to humans by various mechanisms. We considered whether the observed damage to human skeletons at TeH could have resulted from mechanisms other than a cosmic impact event. One co-author is a medical doctor (T.W.) that treated numerous accident victims, many of whom sustained severe multiple traumas and were mangled but always remained intact, including those who exited through windshields and sustained tertiary injuries. Similarly, those who collided with vehicle dashes frequently mangled legs, but only required amputations because artery and nerve supply were damaged beyond repair. Suicide jumpers can reach a terminal velocity of about 53 m/s (118 mph), but that velocity is rare as it requires 50 stories of free fall. Victims of serious falls always arrived at the hospital with multiple fractures (including comminuted and compound) but were intact with no evidence of dismemberment. So, while accidents can produce severe injuries, they pale in comparison to the destructive forces apparent on human bodies at ancient TeH.

Regarding blast wave/blast wind damage, tornadoes are the only naturally occurring phenomenon that even remotely approximates hypersonic blast-wind velocities associated with cosmic impacts. Survivors may be carried many hundreds of feet and are sometimes deposited without any secondary trauma from colliding debris. On the other hand, the remains of some disarticulated victims are sometimes scattered across several square km (Chicago Tribune, May 29, 1997). The longer a body is trapped within the tornado vortex, the more likely it is that blunt-force and penetrating injuries can result in dismemberment and mutilation to the extent that identification is impossible, as reported in the Los Angeles Times, May 30, 1997. However, extreme dismemberment is rare with only one partial amputation due to a laceration in 45 deaths and 690 injuries in a tornado cluster[10]. The vast majority of fatalities (89.5% of 338 reviewed) occurred in the most powerful EF-4 or EF-5 tornadoes[11]. None showed the type of injuries apparent at TeH.

In studying damage to human bodies, the US military has extensively investigated the effects of high explosives, such as improvised explosive devices or IEDs[12]. The blast-wave trauma in humans occurs primarily at bodily interfaces (e.g., air/tissue and tissue/bone junctures), where high-density materials cause the acceleration of shockwaves, followed by their deceleration in lower-density materials. For example, extensive blast damage occurs at air/tissue junctures (e.g., lungs, ears, colon, and the GI tract) where shockwaves reverberate in the air and rupture adjacent bodily structures[12]. Similar interface ruptures also can occur in the liver, spleen, testicles, and brain (white matter/gray matter interface)[13]. Although uncommon, "blow-out" fractures near human eyes can occur as a result of blast waves, which invariably take the path of least resistance and rupture through the egg-shell bone into the maxillary or paranasal sinuses[14].

In the case of damage to humans at TeH, the blast wave from the proposed airburst most likely reflected or echoed off proximal wall surfaces within the city and dramatically amplified bodily injury[15]. Such injuries are commonly lethal but are nearly all internal and thus, would have resulted in only soft-tissue damage. A ten-pound psi overpressure is usually fatal in humans. Higher overpressures, resulting from blast waves of massive energy and/or proximity, would occur during a cosmic airburst and would be capable of dismembering human bodies. In addition, a

sufficiently kinetic blast wave from outside the city could easily entrain debris, including rocks, gravel, sand, and branches. If so, exposed bodies would have been reduced to small bones and fragments, especially during a thermobaric event that would have incinerated soft tissue.

An extremely short duration of exposure to the thermal pulse from explosives can cause superficial, non-lethal, first-degree "flash burns." For longer exposures at close proximity, damage can result in severe third-degree burns. For example, during the detonation of a single kilogram of TNT, instantaneous temperatures can exceed 2800°C[16], and 100 tons of TNT can produce a fireball with temperatures of 8600 K[17]. Both are capable of producing lethal burns.

Regarding the fragmented and pulverized bones, it is difficult to accomplish such destruction without first heating the bones (personal communications to co-author T.W. from crematory operators). Similarly, it is difficult to flay flesh off bones without heating the body (personal experience of T.W.). Furthermore, unheated bones shatter along the longitudinal axis forming splinters yielding a different pattern than that observed at TeH. Extreme temperatures are sufficient, depending on variables of distance, duration, shielding, etc., to cremate flesh, heat bone, and create the results observed at TeH. Parenthetically, perhaps the remarkably preserved below-knee bones pictured in **Fig. 44** of the main manuscript are a result of the victim's leg being buried under debris and thus protected from the burning, flaying, and fragmentation sequence that destroyed the upper part of the victim's body.

An airburst event, such as occurred over Tunguska and Chelyabinsk and similar to that proposed for TeH, produces considerably more damage, especially to humans, than a ground-level explosion because of the 'mach stem' effect, in which the blast wave from an explosion combines with waves reflected off buildings and the Earth's surface, thus increasing the kinetic energy by 2x-9x. Nuclear weapons are typically detonated hundreds of meters above the ground to create maximum damage. Adding a thermal dimension to a bolide airburst blast wave would multiply the human carnage.

ADDITIONAL METHODS

Methods S1. Nanodiamond/diamonoid (ND) extraction protocol for Tall el-Hammam.

Protocol Theory. A general protocol used to isolate NDs from sediments was earlier developed and used successfully for more than 30 sites of Younger Dryas age [18]. That developed protocol was used in this experiment with one necessary modification because of the presence of gypsum-rich sediment samples at this location. Because of the possibility that nanodiamonds were encapsulated by gypsum ($CaSO4 \bullet 2H_2O$) as it formed, gypsum dissolution was necessary to ensure all of the NDs are removed from gypsum binding and thus free to be extracted. Thus, the normal ND extraction protocol was adjusted for a gypsum removal procedure. The protocol both with and without the gypsum removal procedure is shown in **Fig. S10**. The significance of each step in the protocol is discussed below.

NaOH: It has been shown that NDs (in particular those in the YDB layer) contain organic functional groups on their surface[19]. Due to the large amounts of carboxylic acid groups on the surface, the NDs' aqueous solubility can be altered by deprotonation of the carboxyl groups. The NDs' aqueous solubility increases at a pH > 7. Thus, the solution containing the suspended NDs can be extracted. After the supernatant (containing NDs if NDs are present in the samples) was collected, the samples were acidified to remove the carboxyl groups on the surface of the NDs through decarboxylation. As a result, the NDs were no longer suspended, and the samples were centrifuged to collect carbonaceous material.

H_2SO_4: To dissolve gypsum, 0.1 *M* H_2SO_4 was added to the extracted residues to suspend them, then concentrated H_2SO_4 was then added drop-wise to achieve a pH of 0.5-1. After five days, any gypsum initially present was dissolved and the samples were made basic (pH < 7) using 50% NaOH to suspend all nanodiamonds. After centrifugation, supernatants containing suspended nanodiamonds were collected, acidified using 12 M HCl dropwise to a pH of 0.5-1, and centrifuged again to consolidate nanodiamonds into residues.

$K_2Cr_2O_7/H_2SO_4$: The residues were then suspended in 0.5 *M* $K_2Cr_2O_7$/2 *M* H_2SO_4 to oxidize any remaining organic components in the ND-containing containing residue. An example of a redox reaction is shown in Reaction 1, where ethanol is oxidized to acetic acid.

$$4H^+ + Cr_2O_7^{2-} + C_2H_6O \rightarrow 2Cr^{3+} + C_2H_4O_2 + 3H_2O \quad (1)$$

HF/HCl: Silicate residues were then removed using a 10 *M* HF/1 *M* HCl solution. To dissolve fluorides that may have formed, the samples were washed with 9 *M* HCl. The reaction is shown in Reaction 2.

$$4HF + SiO_2 \rightarrow SiF_4 + 2H_2O \quad (2)$$

Protocol Procedure. The following procedure is also depicted schematically in the flowchart of **Fig. S10**. Eight sediment samples (~100 g each) containing primarily sandy quartz were obtained from Allen West. The samples were from different geological areas near the archaeological site of interest. The samples were massed and submerged in 0.1 *M* NaOH (30 mL/10 g) for two days. The samples were then centrifuged at 1000 relative centrifugal force (rcf) for ten minutes (Hermle K 400 Z), and the supernatant was retained for further experimentation. The remaining sediment was treated for gypsum dissolution.

Approximately 10 mL of 0.1 *M* H_2SO_4 was added to the samples undergoing gypsum dissolution. Concentrated H_2SO_4 was then added drop-wise until the pH of each sample was 0.5-1. After five days, the samples were made basic (pH > 7) using 50% NaOH to extract any NDs liberated by gypsum dissolution. The samples were centrifuged at 2500 rcf for ten minutes. The supernatant was collected, and this set of samples was treated identically to the first set of samples for the remaining experimentation. The samples were acidified with approximately 1 mL of 12 *M* HCl to a pH of 0.5-1. The samples were centrifuged for one hour at 2500 rcf. The supernatant was discarded, and the carbonaceous material was collected.

The samples were submerged in 20 mL of 0.5 *M* $K_2Cr_2O_7$/2 *M* H_2SO_4 and placed in a 70°C water bath for twelve days. After twelve days, the samples were rinsed three times using 0.1 *M* HCl. After each rinse, the samples were centrifuged at 2500 rcf for thirty minutes.

To destroy any silicates that may have been present, approximately 7 mL of 10 *M* HF/1 *M* HCl was added to each sample, and then approximately 3 mL of concentrated HF was added. The samples were then diluted with approximately 35 mL of deionized H_2O and centrifuged at 2500 rcf for thirty minutes. To dissolve fluorides that may have formed, approximately 10 mL of 9 *M* HCl was added to each sample. After two days, the samples were diluted with approximately 40 mL of 0.1 *M* HCl and centrifuged at 2500 rcf for one hour. This rinsing process was repeated two more times. The samples were dried and massed. The samples were then analyzed by TEM and SEM.

REFERENCES

1 Metallos. *CaO-Al2O3-SiO2 phase diagram*, <https://el.wikipedia.org/wiki/%CE%91%CF%81%CF%87%CE%B5%CE%AF%CE%BF:CaO-Al2O3-SiO2-phase-diagram-greek.svg> (2007).

2 Hamers, M. & Drury, M. Scanning electron microscope-cathodoluminescence (SEM-CL) imaging of planar deformation features and tectonic deformation lamellae in quartz. *Meteoritics & Planetary Science* **46**, 1814-1831 (2011).

3 Moore, A. M. T. *et al.* Evidence of Cosmic Impact at Abu Hureyra, Syria at the Younger Dryas Onset (~12.8 ka): High-temperature melting at >2200°C. *Sci Rep* **4185** (2020).

4 Bruins, H. J. & Van Der Plight, J. Tell Es-Sultan (Jericho): radiocarbon results of short-lived cereal and multiyear charcoal samples from the end of the Middle Bronze Age. *Radiocarbon* **37**, 213-220 (1995).

5 Weinstein, J. M. Radiocarbon dating in the southern Levant. *Radiocarbon* **26**, 297-366 (1984).

6 Marchetti, N. A century of excavations on the Spring Hill at Tell es-Sultan, ancient Jericho: a reconstruction of its stratigraphy. (University of Rome; Palestinian Dept. of Antiquities, 2000).

7 Collins, G. S., Melosh, H. J. & Marcus, R. Earth impact effects program: a web-based computer program for calculating the regional environmental consequences of a meteoroid impact on Earth. *Meteorit Planet Sci* **40**, 817-840 (2005).

8 Collins, G. S., Melosh, H. J. & Marcus, R. *Earth Impact Effects Program*, <https://impact.ese.ic.ac.uk/ImpactEarth/> (2005).

9 Collins, S. *et al.* The Tall el-Hammam Excavation Project, Season Activity Report, Season Four: 2009 Excavation, Exploration, and Survey. (Department of Antiquities of Jordan, Amman, Jordan, 2009).

10 Brown, S., Archer, P., Kruger, E. & Mallonee, S. Tornado-related deaths and injuries in Oklahoma due to the 3 May 1999 tornadoes. *Weather and Forecasting* **17**, 343-353 (2002).

11 CDC. Tornado-related fatalities--five states, southeastern United States, April 25-28, 2011. *MMWR. Morbidity and mortality weekly report* **61**, 529-533 (2012).

12 Cernak, I. *Gulf War and Health: Long-Term Effects of Blast Exposures*. Vol. 9 (The National Academies Press, 2014).

13 Jorolemon, M. R., Lopez, R. A. & Krywko, D. M. Blast injuries. (2017).

14 Scott, R. The injured eye. *Philosophical Transactions of the Royal Society B: Biological Sciences* **366**, 251-260 (2011).

15 Langhorst, B., Cooka, C., Schondela, J. & Chu, H. Material systems for blast-energy dissipation in *IMPLAST 2010 Conference.* 12-14.

16 Greenwood, J. E. Burn injury and explosions: an Australian perspective. *Eplasty* **9** (2009).

17 Dewey, J. M. The air velocity in blast waves from TNT explosions. *Proceedings of the Royal Society of London. Series A. Mathematical and Physical Sciences* **279**, 366-385 (1964).

18 Kinzie, C. R. *et al.* Nanodiamond-rich layer across three continents consistent with major cosmic impact at 12,800 cal BP. *J Geol* **122**, 475-506 (2014).

19 Shenderova, O. A., Zhirnov, V. V. & Brenner, D. W. Carbon Nanostructures. *Critical Reviews in Solid State and Materials Sciences* **27**, 227-356, doi:10.1080/10408430208500497 (2002).